

Viscoelastic Block Models of the North Anatolian Fault: A Unified Earthquake Cycle Representation of Pre- and Postseismic Geodetic Observations

by Phoebe M. R. DeVries, Plamen G. Krastev, James F. Dolan, and Brendan J. Meade

Abstract Along the North Anatolian fault (NAF), the surface deformation associated with tectonic block motions, elastic strain accumulation, and the viscoelastic response to past earthquakes has been geodetically observed over the last two decades. These observations include campaign-mode Global Positioning System (GPS) velocities from the decade prior to the 1999 M_w 7.4 İzmit earthquake and seven years of continuously recorded postseismic deformation following the seismic event. Here, we develop a 3D viscoelastic block model of the greater NAF region, including the last 2000 yrs of earthquake history across Anatolia, to simultaneously explain geodetic observations from both before and after the İzmit earthquake. With a phenomenologically motivated simple two-layer structure (schizosphere and plastosphere) and a Burgers rheology (with Maxwell viscosity $\log_{10} \eta_M \approx 18.6\text{--}19.0$ Pa·s and Kelvin viscosity $\log_{10} \eta_K \approx 18.0\text{--}19.0$ Pa·s), a block model that incorporates tectonic plate motions, interseismic elastic strain accumulation, transient viscoelastic perturbations, and internal strain can explain both the pre- and post-İzmit earthquake observations with a single unified model. Viscoelastic corrections to the interseismic GPS velocity field with the unified model reach magnitudes of ~ 2.9 mm/yr. Geodetically constrained slip-deficit rate estimates along the central NAF and northern strand of the NAF in the Sea of Marmara vary nonmonotonically with Maxwell viscosity and change by up to 23% (~ 4 mm/yr) for viscosities ranging from 10^{18} to 10^{23} Pa·s. For the best-fit viscosity structures, central NAF slip-deficit rates reach 22 mm/yr, increasing to 28 mm/yr in the Sea of Marmara. Along the central NAF, these rates are similar to the fastest geologic slip-rate estimates. The fastest slip-deficit rate estimates along the entire fault system ($\sim 27\text{--}28$ mm/yr) occur less than 50 km from Istanbul, along the northern strand of the NAF in the Sea of Marmara.

Electronic Supplement: Figure of sensitivity of viscoelastic block model slip-deficit rate estimates and contour plot of mean residual improvement.

Introduction

Existing models of earthquake cycle deformation are largely focused on either explaining postseismic geodetic observations from the first 1–10 yrs after large ($M_w > 6.5$) earthquakes (e.g., Reilinger *et al.*, 2000; Bürgmann *et al.*, 2002; Ergintav *et al.*, 2002, 2009; Hearn *et al.*, 2002; Ryder *et al.*, 2007, 2011), or explaining observations of nominally interseismic deformation occurring long after (> 10 yrs) an earthquake (e.g., Savage and Burford, 1973). To gain a more complete understanding of the earthquake cycle, postseismic and interseismic geodetic observations must be integrated and explained with a unified model that can provide a physical

explanation for both rapid postseismic deformation and more slowly varying interseismic deformation (Hetland, 2006; Hearn *et al.*, 2009; DeVries and Meade, 2013; Meade *et al.*, 2013; Yamasaki *et al.*, 2014; Hearn and Thatcher, 2015).

Geodetic observations across strike-slip faults from both before and after large earthquakes exist along the San Andreas fault (SAF) at Parkfield (e.g., Bakun and Lindh, 1985), across the Kunlun fault in Tibet (Bell *et al.*, 2011; Zhang *et al.*, 2004, 2009; Ryder *et al.*, 2007, 2011), and along the North Anatolian fault (NAF) in Turkey (Fig. 1; Reilinger *et al.*, 1997, 2006; Bürgmann *et al.*, 2002; Ergintav *et al.*, 2002, 2009). These

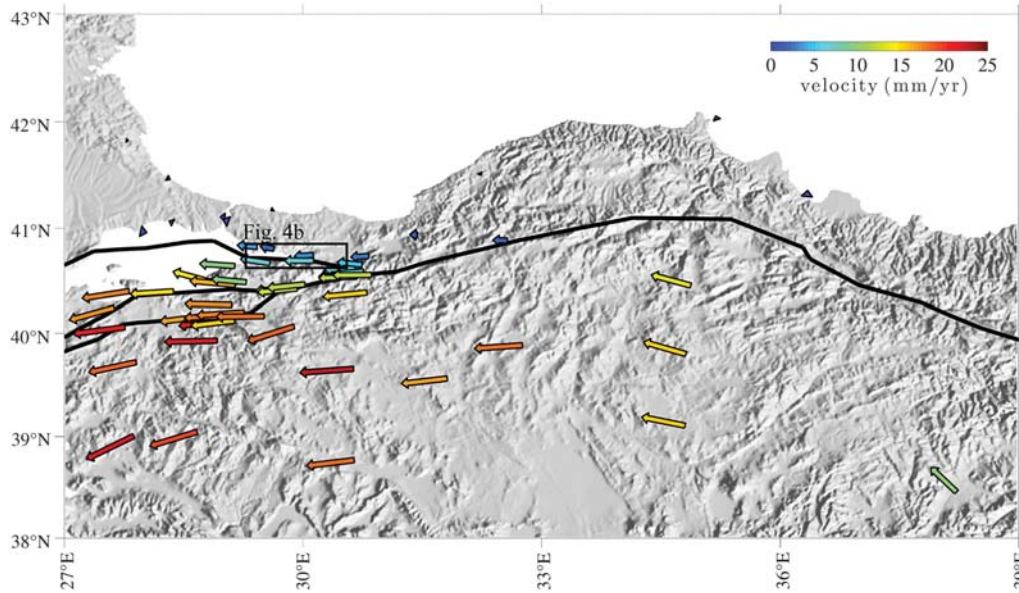


Figure 1. Interseismic Global Positioning System (GPS) velocities (Reilinger *et al.*, 2006) and shaded relief map of Turkey. Velocities are shown in a nominally Eurasian reference frame and are color coded by magnitude with warmer colors indicating faster velocities. The trace of the North Anatolian fault (NAF) is shown with a thick black line. The black box over the northern strand of the NAF on the western edge of the figure highlights the area shown in Figure 4b; the 1999 M_w 7.4 İzmit earthquake ruptured the segments of the fault within the black box.

pre- and postseismic observations represent an opportunity to constrain models of the earthquake cycle on strike-slip faults worldwide.

The Global Positioning System (GPS) observations across the NAF exhibit dense spatial and temporal coverage. The easternmost and westernmost sections of the NAF were widely recognized as seismic gaps prior to the 1999 M_w 7.4 İzmit earthquake (Toksöz *et al.*, 1979; Barka, 1992, 1996; Stein *et al.*, 1997) and as a result, survey-mode GPS campaigns were conducted in eastern Turkey and the Sea of Marmara region in the decade before the earthquake (Reilinger *et al.*, 1997, 2006; Straub *et al.*, 1997; McClusky *et al.*, 2000). In addition, several permanent GPS stations were installed to continuously record deformation (Ergintav *et al.*, 2002). These observations together revealed a localized velocity gradient with a differential velocity of ~ 24 mm/yr over a 200-km-wide transect across the western strand of the NAF in the Sea of Marmara region prior to the 1999 earthquake (Fig. 1; Bürgmann *et al.*, 2002; Meade *et al.*, 2002). Elastic block models incorporating these pre-earthquake velocities provide fault-slip-deficit rate constraints (sometimes termed geodetic slip-rate constraints) of ~ 24 – 30 mm/yr along the NAF, with rates increasing westward along the main northern strand of the NAF in the Sea of Marmara region (Reilinger *et al.*, 1997, 2006; McClusky *et al.*, 2000; Meade *et al.*, 2002).

Postseismic GPS displacements immediately following the 1999 İzmit earthquake have been effectively explained by aseismic afterslip down-dip of the coseismic rupture zone with maximum slip of about 43 cm over a 75-day period (Reilinger *et al.*, 2000). Time-dependent analysis of GPS

position time series in the 87 days after the İzmit earthquake suggests that maximum aseismic slip rates may have reached 2 m/yr (Bürgmann *et al.*, 2002). A weakly velocity strengthening ($a-b = 0.19$ MPa) frictional afterslip model has also been used to explain the GPS displacements in the 80 days immediately after the İzmit earthquake (Hearn *et al.*, 2002). Over a longer observation period from 1999 to 2003, three logarithmic decay constants have been used to fit the displacement time series observed at continuous GPS stations (Ergintav *et al.*, 2002, 2009). Postseismic time series from the four years immediately after the İzmit earthquake have also been explained by a combination of frictional afterslip during the first few months after the earthquake, and viscoelastic deformation with a Maxwell rheology with viscosity $\eta_M = 2$ – 5×10^{19} Pa·s for the remainder of this observational interval (Hearn *et al.*, 2009). Another study (Wang *et al.*, 2008) incorporates a standard linear solid rheology to explain the İzmit postseismic observations.

To understand the NAF earthquake cycle to an even greater extent, both the pre- and postearthquake data have to be examined and explained simultaneously. This was first recognized after the İzmit earthquake (Hetland, 2006), and in 2D, GPS data from both before and after the 1999 M_w 7.4 İzmit earthquake have been successfully explained with a two-layer Burgers model with a transient (Kelvin) relaxation timescale ($\tau_K = \eta_K/\mu_K$) of 2–5 yrs and a steady (Maxwell) timescale ($\tau_M = \eta_M/\mu_M$) of more than 400 yrs (Hetland, 2006). More recently, models incorporating shear zones (24–40 km in width) extending to midcrustal depths with low viscosities ($\sim 2 \times 10^{18}$ Pa·s) in the shear zone and higher viscosities ($> 2 \times 10^{20}$ Pa·s) in the surrounding medium have been used

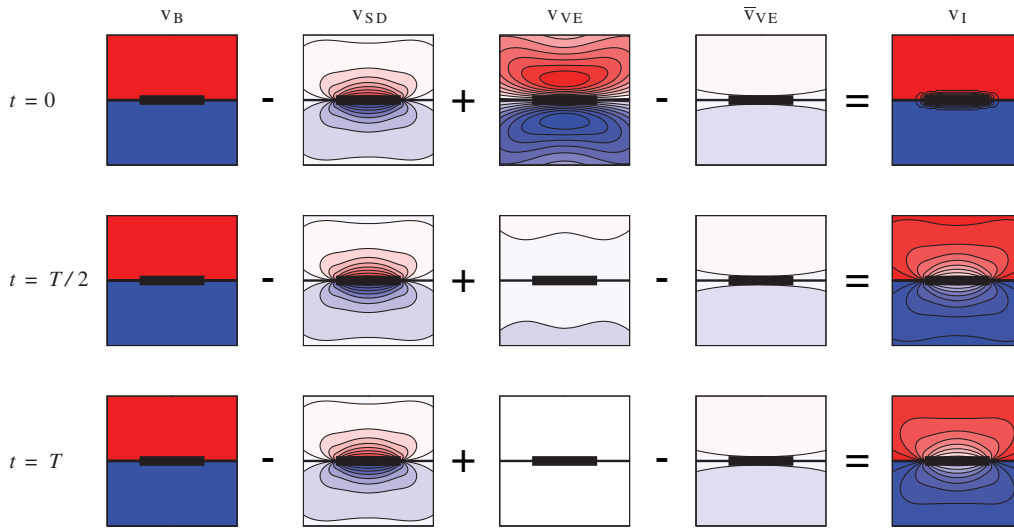


Figure 2. The components of a velocity field in a viscoelastic block model framework (equation 2) at three times through the earthquake cycle. Interseismic velocities \mathbf{v}_I are modeled as the sum of the velocities due to long-term block motion \mathbf{v}_B , the velocities due to the accumulated slip deficit \mathbf{v}_{SD} , the viscoelastic effects of the most recent earthquake \mathbf{v}_{VE} along the fault segment, and the mean velocity throughout the earthquake cycle velocity $\bar{\mathbf{v}}_{VE}$. For simplicity, the velocities due to homogenous internal strain of the blocks $\mathbf{v}_{\dot{\epsilon}}$ are not included in this schematic diagram.

to explain GPS observations in the Sea of Marmara region from both before the İzmit earthquake and six months of post-seismic deformation after the event (Yamasaki *et al.*, 2014). In another recent study (Hearn and Thatcher, 2015), crust- to lithosphere-scale viscous shear zones with effective viscosity-per-unit width in the zones increasing from $(\eta_{sz}/w) \approx 10^{15}$ Pa·s/m in the crust to $(\eta_{sz}/w) \geq 5 \times 10^{16}$ Pa·s/m below the Moho were found to explain pre- and postearthquake deformation. In these preferred models, the shear zones cut through a strong ($\eta > 10^{20}$ Pa·s) lithosphere and a weaker asthenosphere ($\eta < 10^{19}$ Pa·s) (Hearn and Thatcher, 2015).

The previous earthquake cycle models of the NAF described above (Hetland, 2006; Yamasaki *et al.*, 2014) have taken into account repeated earthquakes on the İzmit strand of the western NAF. Here, we develop a 3D viscoelastic block model of the greater NAF region, taking into account the last 2000 yrs of earthquake history (e.g., Barka, 1992, 1996; Ambraseys and Jackson, 2000; Ambraseys, 2002) to assess in an internally consistent manner whether or not both pre- and postearthquake deformation along the NAF can be simultaneously explained with a single rheological model. We also examine the sensitivity of geodetic slip-deficit rate estimates to the assumed viscosity structure and compare these slip-deficit rates from geodetically constrained viscoelastic block models with Holocene slip-rate estimates along the NAF based on offset geomorphic features (e.g., Hubert-Ferrari *et al.*, 2002; Kondo *et al.*, 2004; Kozacı *et al.*, 2007, 2009; Pucci *et al.*, 2008; Dolan, 2009; Uçarkuş [unpublished thesis, 2010; see Data and Resources]; Meghraoui *et al.*, 2012).

Viscoelastic Block Model

In classical elastic block theory (Matsu'ura *et al.*, 1986; McCaffrey, 2002; Meade and Hager, 2005; Meade and Love-

less, 2009), interseismic velocities \mathbf{v}_I are modeled as the sum of the velocities due to long-term block motion \mathbf{v}_B , the velocities due to the accumulated slip deficit \mathbf{v}_{SD} , and the velocities due to internal strain of the blocks $\mathbf{v}_{\dot{\epsilon}}$:

$$\mathbf{v}_I = \mathbf{v}_B - \mathbf{v}_{SD} + \mathbf{v}_{\dot{\epsilon}}. \quad (1)$$

To incorporate the viscoelastic earthquake cycle effects of past earthquakes into 3D kinematically consistent block models (Sato and Matsu'ura, 1988; Smith and Sandwell, 2006; Johnson *et al.*, 2007; Pollitz *et al.*, 2008, 2010; Hilley *et al.*, 2009; Chuang and Johnson, 2011; Hearn *et al.*, 2013; Tong *et al.*, 2014), a viscoelastic correction must be taken into account. The correction consists of two components: (1) the viscoelastic effects of the most recent earthquake \mathbf{v}_{VE} along the fault segment and (2) the mean velocity throughout the earthquake cycle $\bar{\mathbf{v}}_{VE}$. In a viscoelastic block model framework, modeled interseismic velocities are composed of five components (Fig. 2):

$$\mathbf{v}_I = \mathbf{v}_B - \mathbf{v}_{SD} + \mathbf{v}_{\dot{\epsilon}} + \mathbf{v}_{VE}(\eta_M, \eta_K, t - t_{eq}) - \bar{\mathbf{v}}_{VE}(\eta_M, \eta_K, T). \quad (2)$$

The first term of the viscoelastic correction, the viscoelastic effect of the most-recent earthquake, depends on the time since the most-recent earthquake $t - t_{eq}$ and the assumed viscosities η_M and η_K . The mean earthquake cycle velocity term, the second term in the correction, depends on the assumed recurrence interval T and viscosities η_M and η_K . This construction ensures that over many earthquake cycles, the displacements everywhere are equal to the long-term block displacements. In classic block theory (Matsu'ura *et al.*, 1986; McCaffrey, 2002; Meade and Hager, 2005; Meade and Loveless, 2009), this is referred to as kinematic consistency.

Fault-slip-deficit rates constrained by an elastic block model are kinematically consistent because they are linearly proportional to differential block motions.

However, in a viscoelastic block model framework, the concept of kinematic consistency is more complicated and may be divided into two distinct components, which we term type I and type II kinematic consistency. To satisfy type I kinematic consistency, fault-slip-deficit rates must be linearly proportional to differential block motions, just as in elastic block models. Type II kinematic consistency is related to the assumptions implicit in the viscoelastic correction term $\mathbf{v}_{\text{VE}}(\eta_{\text{M}}, \eta_{\text{K}}, t - t_{\text{eq}}) - \bar{\mathbf{v}}_{\text{VE}}(\eta_{\text{M}}, \eta_{\text{K}}, T)$ in equation (2). To calculate this viscoelastic correction, we assume a characteristic slip s and recurrence interval T for the earthquake and therefore implicitly assume a long-term slip rate of s/T on the fault. In order for a viscoelastic block model to satisfy type II kinematic consistency, the final slip-deficit rate estimate from viscoelastic block models must be equal to the long-term slip rate s/T that we assume in the viscoelastic corrections. Constructing a viscoelastic model that satisfies type II kinematic consistency and is as consistent as possible with the timing and estimated magnitudes of historic earthquakes would require an iterative method, in which we would assume a long-term slip rate consistent with geologic estimates of s and T and then incrementally iterate these values until we approach s_{II} and T_{II} , the values of s and T for which s/T is equivalent to the final viscoelastic block model slip-deficit rate estimates. In a viscoelastic block model that satisfies the conditions of both type I and type II kinematic consistency, the assumed long-term slip rate $s_{\text{II}}/T_{\text{II}}$ may or may not be consistent with geologic constraints on s and T . The viscoelastic block models in this article automatically satisfy type I kinematic consistency (e.g., Meade and Loveless, 2009), but here we choose to be as consistent as possible with geologic estimates of s and T along the NAF (Barka, 1992, 1996, 1999; Ambraseys and Jackson, 2000, Ambraseys, 2002) at the cost of type II kinematic consistency.

To show the construction of the viscoelastic block model in more detail, we can rewrite the right side of equation (2) in a block model framework:

$$\mathbf{v}_{\text{I}} = [\mathbf{G}_{\text{B}} - \mathbf{G}_{\text{SD}}]\mathbf{\Omega} + \mathbf{G}_{\text{E}}\dot{\mathbf{e}} + \mathbf{v}_{\text{VE}}(\eta_{\text{M}}, \eta_{\text{K}}, t - t_{\text{eq}}) - \bar{\mathbf{v}}_{\text{VE}}(\eta_{\text{M}}, \eta_{\text{K}}, T). \quad (3)$$

The matrix–vector products give the contributions of block rotation, slip-deficit, and homogenous internal block strain to the velocity field. Assuming that the viscoelastic contributions are functions of past earthquake activity only, we can rewrite equation (3) as

$$\mathbf{v}_{\text{I}} - \mathbf{v}_{\text{VE}}(\eta_{\text{M}}, \eta_{\text{K}}, t - t_{\text{eq}}) + \bar{\mathbf{v}}_{\text{VE}}(\eta_{\text{M}}, \eta_{\text{K}}, T) = [\mathbf{G}_{\text{B}} - \mathbf{G}_{\text{SD}}]\mathbf{\Omega} + \mathbf{G}_{\text{E}}\dot{\mathbf{e}}. \quad (4)$$

Generalizing this framework to incorporate the viscoelastic effects of N_{eq} periodic earthquakes on different fault seg-

ments requires only a summation over all of the individual earthquakes, because the rheologies considered here are linear:

$$\mathbf{v}_{\text{I}} - \sum_{i=1}^{N_{\text{eq}}} [\mathbf{v}_{\text{VE}}^i(\eta_{\text{M}}, \eta_{\text{K}}, t - t_{\text{eq}}^i) - \bar{\mathbf{v}}_{\text{VE}}^i(\eta_{\text{M}}, \eta_{\text{K}}, T_i)] = [\mathbf{G}_{\text{B}} - \mathbf{G}_{\text{SD}}]\mathbf{\Omega} + \mathbf{G}_{\text{E}}\dot{\mathbf{e}}. \quad (5)$$

This can be rewritten as

$$\mathbf{v}_{*}(\eta_{\text{M}}, \eta_{\text{K}}) = [\mathbf{G}_{\text{B}} - \mathbf{G}_{\text{SD}}]\mathbf{\Omega} + \mathbf{G}_{\text{E}}\dot{\mathbf{e}}, \quad (6)$$

in which

$$\mathbf{v}_{*}(\eta_{\text{M}}, \eta_{\text{K}}) = \mathbf{v}_{\text{I}} - \sum_{i=1}^{N_{\text{eq}}} [\mathbf{v}_{\text{VE}}^i(\eta_{\text{M}}, \eta_{\text{K}}, t - t_{\text{eq}}^i) - \bar{\mathbf{v}}_{\text{VE}}^i(\eta_{\text{M}}, \eta_{\text{K}}, T_i)]. \quad (7)$$

Equation (6) is a classic block model problem (e.g., Meade and Loveless, 2009) with a velocity field $\mathbf{v}_{*}(\eta_{\text{M}}, \eta_{\text{K}})$ modified to correct for the viscoelastic effects of N_{eq} sets of periodic earthquakes. With this framework, it is straightforward to construct a viscoelastic block model incorporating the effects of many ancient and historic earthquakes: we calculate the viscoelastic effects from previous earthquakes $\sum_{i=1}^{N_{\text{eq}}} [\mathbf{v}_{\text{VE}}^i(\eta_{\text{M}}, \eta_{\text{K}}, t - t_{\text{eq}}^i) - \bar{\mathbf{v}}_{\text{VE}}^i(\eta_{\text{M}}, \eta_{\text{K}}, T_i)]$ and then combine these viscoelastic velocities with the observed interseismic GPS velocities to calculate $\mathbf{v}_{*}(\eta_{\text{M}}, \eta_{\text{K}})$ as

$$\mathbf{v}_{*}(\eta_{\text{M}}, \eta_{\text{K}}) = \mathbf{v}_{\text{GPS}} - \sum_{i=1}^{N_{\text{eq}}} [\mathbf{v}_{\text{VE}}^i(\eta_{\text{M}}, \eta_{\text{K}}, t - t_{\text{eq}}^i) - \bar{\mathbf{v}}_{\text{VE}}^i(\eta_{\text{M}}, \eta_{\text{K}}, T_i)]. \quad (8)$$

The 3D calculations of $\mathbf{v}_{\text{VE}}^i(\eta_{\text{M}}, \eta_{\text{K}}, t - t_{\text{eq}}^i)$ and $\bar{\mathbf{v}}_{\text{VE}}^i(\eta_{\text{M}}, \eta_{\text{K}}, T_i)$ are based on the spectral propagator matrix approach (Sato, 1971; Sato and Matsu'ura, 1973, 1988; Matsu'ura and Sato, 1975, 1989; Fukahata and Matsu'ura, 2005, 2006; Hashima *et al.*, 2014) to calculate strains, stresses, velocities, and displacements at depth due to point-source dislocations embedded within a vertically layered half-space. The model can incorporate an arbitrary number of viscoelastic layers, and earthquake sources may be in both elastic and viscoelastic layers. The viscoelastic layers may have either Maxwell or Burgers (transient) rheologies (e.g., Pollitz, 1992; Chopra, 1997; Hetland, 2006; Hetland and Hager, 2006; Meade *et al.*, 2013).

The time-dependent viscoelastic response is calculated using the correspondence principle, which allows any linear viscoelastic problem to be written in the form of an elastic problem in the Laplace domain (e.g., Nur and Mavko, 1974; Savage and Prescott, 1978; de Hoog *et al.*, 1982; Hetland and Hager, 2005).

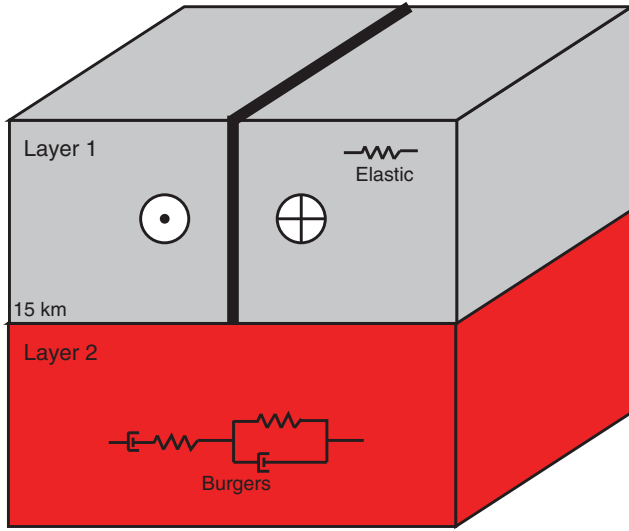


Figure 3. Model geometry cross section and rheologies used in this study.

To approximate finite rupture sources, we integrate over point sources using a 2D Legendre–Gaussian quadrature rule (e.g., Hildebrand, 1987). The deformation due to each point source can be simply summed with Gaussian weights to obtain the deformation due to a finite source. The number of earthquake sources (n^2) required to accurately represent a particular finite source is based on a heuristic scaling $n = cL/d$ (Klöckner *et al.*, 2013), in which d is the distance of the closest observation point to the finite source, L is the length of the finite source, and c is a constant. We use $c = 3$, a value at which the mean percentage difference in displacement magnitude from an equivalent elastic finite source solution (Okada, 1992) is $<0.2\%$ immediately after an earthquake in a square area of $2L \times 2L$ around the fault at the surface.

Here, we use an idealized two-layer rheology structure (schizosphere and plastosphere), in which the upper elastic layer is 15 km thick, and earthquakes rupture through this entire layer. The lower layer is a Burgers viscoelastic half-space with a transient Kelvin viscosity η_K and a long-term Maxwell viscosity η_M (Fig. 3). Elastic moduli of $\lambda = \mu = 3 \times 10^{10}$ Pa are assumed in the elastic layer and in the Burgers viscoelastic layer. More complicated models incorporating three rheological layers and viscous shear zones have been considered in the previous studies of post-seismic deformation along the NAF (e.g., Hearn *et al.*, 2009; Yamasaki *et al.*, 2014; Hearn and Thatcher, 2015). Here, the use of a simple two-layer model is phenomenologically motivated, as we are interested in finding the simplest model that can explain the available data. In 2D, this two-layer model can explain the agreement between geodetic slip-deficit rates and geologic slip-rate estimates across 15 strike-slip faults worldwide (Meade *et al.*, 2013).

To do these calculations in practice, we rotate each fault segment into an oblique Mercator projection so that its strike is parallel to the x axis and calculate the viscoelastic effects

of the earthquakes along individual fault segments $\mathbf{v}_{VE}^i(\eta_M, \eta_K, t - t_{eq}^i)$ (Meade and Loveless, 2009). The mean earthquake cycle velocities $\bar{\mathbf{v}}_{VE}^i(\eta_M, \eta_K, T_i)$ are given by the difference between the displacements d at the beginning and end of the earthquake cycle divided by the duration of the earthquake cycle T_i :

$$\bar{\mathbf{v}}_{VE}^i(\eta_M, \eta_K, T_i) = \frac{d_{VE}^i(\eta_M, \eta_K, T_i) - d_{VE}^i(\eta_M, \eta_K, 0)}{T_i}. \quad (9)$$

The North Anatolian Fault

Geodetic Observations of Preseismic and Postseismic Deformation

In anticipation of potential future earthquakes, survey-mode GPS campaigns were conducted around the western part of the NAF in the Sea of Marmara region in the decade before the İzmit earthquake. The pre-earthquake velocity field used here consists of 122 stations (Fig. 1; Reilinger *et al.*, 2006). For simplicity, we treat this campaign-mode velocity field observed from 1988 to 1999 as representative of the instantaneous velocity field on 1 January 1997. Additionally, a few permanent GPS stations were recording deformation at the time of the İzmit earthquake (Ergintav *et al.*, 2009) and continued to record postseismic deformation after the earthquake. Immediately after the earthquake, more continuous stations were deployed (Ergintav *et al.*, 2009). A 7-yr position time series has been published from GPS station TUBI. This station was moving steadily prior to the earthquake (Fig. 4a,b; from fig. 4a of Ergintav *et al.*, 2009). In the weeks immediately after the earthquake, the station moved rapidly (> 100 mm/yr) to the east, but its eastward velocity decayed to ~ 10 mm/yr after two years (Fig. 4).

Because a linear interseismic trend has been subtracted from the TUBI time series (Ergintav *et al.*, 2002, 2009) (Fig. 4a), this time series records a postseismic perturbation to steady interseismic motion. In other words, if we integrate equation (2) in time, we obtain displacements

$$\mathbf{d}(t) = \mathbf{v}_B t - \mathbf{v}_{SD} t + \mathbf{v}_e t + \int_0^t \mathbf{v}_{VE}(\eta_M, \eta_K, t - t_{eq}) dt - \bar{\mathbf{v}}_{VE}(\eta_M, \eta_K, T) t. \quad (10)$$

The linear terms $\mathbf{v}_B t$, $\mathbf{v}_{SD} t$, $\mathbf{v}_e t$, and $\bar{\mathbf{v}}_{VE}(\eta_M, \eta_K, T) t$ have been subtracted from the time series (Fig. 4b), so we compare the TUBI position time series in the east direction with $d_{VE}^{\{east\}}(t) = \int_0^t v_{VE}^{\{east\}}(\eta_M, \eta_K, t - t_{eq}) dt$, the eastward displacements due to only the viscoelastic perturbation term. We do not take into account the (nonlinear) viscoelastic effects of the historic earthquakes in Figure 5 on the TUBI time series for simplicity and because the 1999 İzmit earthquake dominates the nonlinear viscoelastic signal. Across all viscosity structures tested, the maximum east displacement due to

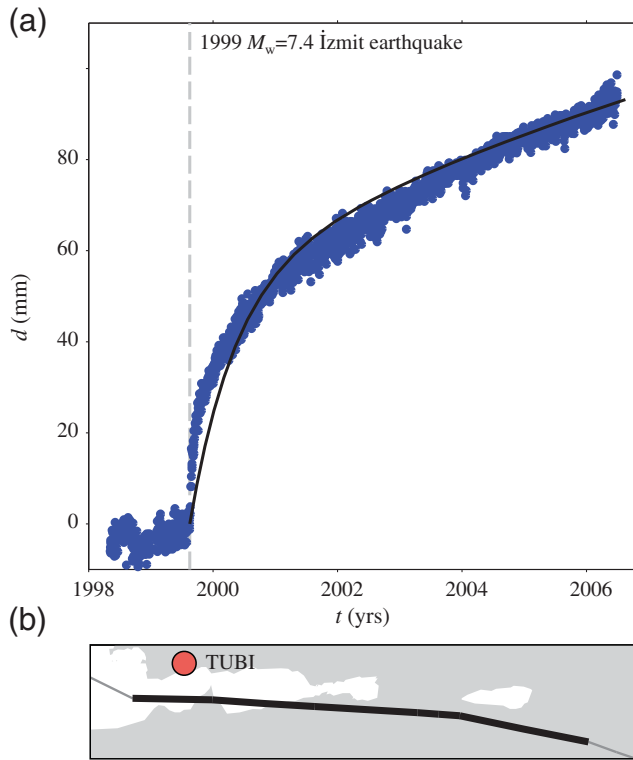


Figure 4. (a) Position time series from GPS station TUBI for the year and a half before and seven years after the 1999 M_w 7.4 İzmit earthquake (from fig. 4a of [Ergintav et al., 2009](#)). Vertical gray dashed line indicates the time of the earthquake. The black line shows the model that best explains the time series, a Maxwell viscosity $\eta_M = 10^{18.6}$ Pa·s and a Kelvin viscosity $\eta_K = 10^{18.0}$ Pa·s, assuming uniform slip of 2.83 m. (b) Modeled rupture extent of the 1999 M_w 7.4 İzmit earthquake and the location of TUBI.

$d_{VE}^{(east)}(t = 2007)$ from the penultimate earthquake, in 1967, is 2.4 mm, <3% of the total displacement at TUBI.

Earthquake History along the NAF

Because the region was colonized by the Greeks in the seventh century B.C.E. and was the seat of the Roman, Byzantine, and Ottoman Empires since the fourth century C.E., the earthquake history along the western NAF over the past 2000 yrs is relatively well known from written records ([Ambraseys, 2002](#)). In the Sea of Marmara region in particular, 55 $M_s \geq 6.8$ earthquakes have been identified since 1 B.C.E. ([Ambraseys, 2002](#)). For the purposes of this article, we have included the effects of the earthquakes that likely occurred along the strands included in the block model geometry (Fig. 5; [Ambraseys and Jackson, 2000](#); [Ambraseys, 2002](#)). The block geometry (Fig. 1) is based on a detailed fault map of Turkey (R. Reilinger, personal comm., 2013). The historic earthquakes included in the viscoelastic block models and their parameters are listed in Table 1. The effects of the 1949, 1992, 1971, and 1966 earthquakes are not included because they occurred to the east of our study area, beyond the eastern extent of the 1939 rupture ([Barka, 1992, 1996](#); [Stein et al., 1997](#)).

For segments of the NAF that have ruptured multiple times over the past two millennia, we use the timing of the repeated ruptures to estimate characteristic recurrence intervals. There are records of earthquakes occurring near the 1999 İzmit earthquake in 68, 268, 478, 1719, and 1894 ([Ambraseys, 2002](#); [Drab et al., 2015](#)). Based on the more recent events, we use a recurrence interval of $T = 100$ yrs for these İzmit-like earthquakes. For fault segments in the Sea of Marmara region without a recorded pattern of repeated ruptures, we assume $T = 500$ yrs. The exceptions are the 1 B.C.E. and 121 C.E. earthquakes, for which we assume recurrence intervals of 2050 yrs, and the 1296 and 1419 events, for which we assume recurrence intervals of 1000 yrs, assuming that they may reoccur soon but have not done so yet. Along the central NAF, prior to the 1999 event, seven earthquakes of $M_w > 6.8$ have ruptured the fault in 1939, 1942, 1943, 1944, 1951, 1957, and 1967, largely from east to west. Based on earthquake history along the central NAF ([Barka, 1992, 1996](#)), we use $T = 400$ yrs for these most recent earthquakes.

The average slip magnitude estimates for earthquakes that occurred before 1939 are based on estimated surface-wave magnitudes ([Ambraseys and Jackson, 2000](#); [Ambraseys, 2002](#)). We treat these surface-wave magnitudes as proxies for moment magnitudes and calculate average slip using a shear modulus of $\mu = 3 \times 10^{10}$ and the fault geometry in Figure 1. For the 1894 earthquake, we assume the moment magnitude of the 1999 İzmit earthquake (M_w 7.4; [Barka, 1999](#); [Ambraseys, 2001](#)). For the earthquakes from 1939 to 1967, we calculate the average slip for each earthquake using the seismic moments reported in previous viscoelastic studies of the NAF ([Lorenzo-Martín et al., 2006](#)). We assume uniform slip along the entire length of each historical rupture (Table 1).

We have also included hypothetical ancient earthquakes at 1 B.C.E. on two segments of the two southern strands of the NAF in the Sea of Marmara (Fig. 5; Table 1). The removal of these hypothetical earthquakes from the models does not substantially change the conclusions in this article. However, because these fault segments are in a tectonically active region and to our knowledge there is no evidence that they accommodate substantial creep or have ruptured in recent historical earthquakes ([Ambraseys and Jackson, 2000](#); [Ambraseys, 2002](#)), we assume that they have ruptured within the last few thousand years and may now be late in the earthquake cycle.

Viscoelastic Modeling of the NAF Earthquake Cycle

Modeling the Postseismic Data from GPS Station TUBI

We found the viscosity structure that best explains the postseismic GPS data from TUBI, a Maxwell viscosity $\eta_M = 10^{18.6}$ Pa·s and a Kelvin viscosity $\eta_K = 10^{18.0}$ Pa·s (Fig. 4a), by a grid search over Maxwell and Kelvin viscosities in the $10^{17.0}$ to $10^{23.0}$ Pa·s range. We present residuals in terms of a mean residual improvement (MRI) percentage over an elastic model:

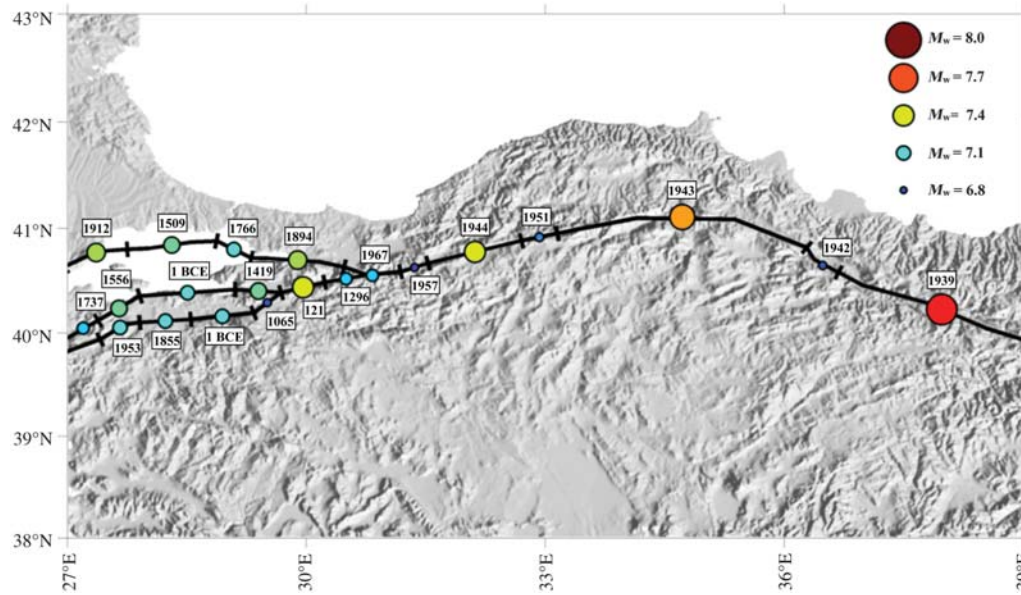


Figure 5. Map of the locations and sizes of the historic earthquakes included in the viscoelastic block models. For the purposes of this article, we have included the effects of only the historical earthquakes that likely occurred along the strands included in the block model geometry (Barka, 1992, 1996; Ambraseys and Jackson, 2000; Ambraseys, 2002). The detailed model parameters of these earthquakes are listed in detail in Table 1.

$$\text{MRI}(\eta_M, \eta_K) = \frac{-(\overline{|\mathbf{r}_{VE}(\eta_M, \eta_K)|} - \overline{|\mathbf{r}_E|})}{\overline{|\mathbf{r}_E|}} \times 100 \quad (11)$$

(Fig. 6a), in which $\mathbf{r}_{VE}(\eta_M, \eta_K)$ are the residuals for the viscoelastic models with viscoelastic parameters η_M, η_K , and \mathbf{r}_E are the residuals for an elastic model. Models that explain the

data better than an elastic model will have a large and positive MRI; models that do not explain the data as well as an elastic model will have a negative MRI. In the case of the TUBI postseismic data, $\overline{|\mathbf{r}_{VE}|}$ is the mean of the absolute values of the displacements (67.5 mm) because the displace-

Table 1
Detailed Parameters of the Earthquakes Taken into Account in the Viscoelastic Block Models

	Length of Rupture (km)	M_0 (N·m)	M_w	Average Slip (m)	Recurrence Interval (yr)	References
1 January 1 B.C.E. (south)	67	3.16×10^{19}	7.0	1.0437	2050	*
1 January 1 B.C.E. (north)	102	3.16×10^{19}	7.0	0.6910	2050	*
1 January 121	48	1.26×10^{20}	7.4	5.8822	2050	Ambraseys and Jackson (2000) and Ambraseys (2002)
1 September 1065	36	1.59×10^{19}	6.8	0.9652	1000	Ambraseys and Jackson (2000) and Ambraseys (2002)
1 June 1296	46	3.16×10^{19}	7.0	1.5354	1000	Ambraseys and Jackson (2000) and Ambraseys (2002)
15 March 1419	49	6.31×10^{19}	7.2	2.8636	1000	Ambraseys and Jackson (2000) and Ambraseys (2002)
10 September 1509	95	6.31×10^{19}	7.2	1.4772	600	Ambraseys and Jackson (2000) and Ambraseys (2002)
10 May 1556	52	6.31×10^{19}	7.2	2.7174	600	Ambraseys and Jackson (2000) and Ambraseys (2002)
6 March 1737	37	3.16×10^{19}	7.0	1.8893	500	Ambraseys and Jackson (2000) and Ambraseys (2002)
22 May 1766	40	4.47×10^{19}	7.1	2.4295	500	Ambraseys and Jackson (2000) and Ambraseys (2002)
5 August 1766	54	1.26×10^{20}	7.4	5.1916	500	Ambraseys and Jackson (2000) and Ambraseys (2002)
28 February 1855	55	4.47×10^{19}	7.1	1.8175	500	Ambraseys and Jackson (2000) and Ambraseys (2002)
10 July 1894	99	8.91×10^{19}	7.3	2.8259	100	Barka (1999)
9 August 1912	70	8.91×10^{19}	7.3	2.8471	400	Ambraseys and Jackson (2000) and Ambraseys (2002)
26 December 1939	263	4.11×10^{20}	7.7	3.4679	400	Barka (1992, 1996) and Lorenzo-Martín <i>et al.</i> (2006)
20 December 1942	44	1.74×10^{19}	6.8	0.8776	400	Barka (1992, 1996) and Lorenzo-Martín <i>et al.</i> (2006)
26 November 1943	270	2.51×10^{20}	7.6	2.0665	400	Barka (1992, 1996) and Lorenzo-Martín <i>et al.</i> (2006)
1 February 1944	101	1.48×10^{20}	7.4	3.2406	400	Barka (1992, 1996) and Lorenzo-Martín <i>et al.</i> (2006)
13 August 1951	38	2.12×10^{19}	6.9	1.2237	400	Barka (1992, 1996) and Lorenzo-Martín <i>et al.</i> (2006)
8 March 1953	47	4.47×10^{19}	7.1	2.1193	400	Ambraseys and Jackson (2000) and Ambraseys (2002)
26 May 1957	31	1.35×10^{19}	6.7	0.9781	400	Barka (1992, 1996) and Lorenzo-Martín <i>et al.</i> (2006)
22 July 1967	61	2.82×10^{19}	7.0	1.0186	400	Barka (1992, 1996) and Lorenzo-Martín <i>et al.</i> (2006)

*Hypothetical ancient earthquakes that are not in the historic record.

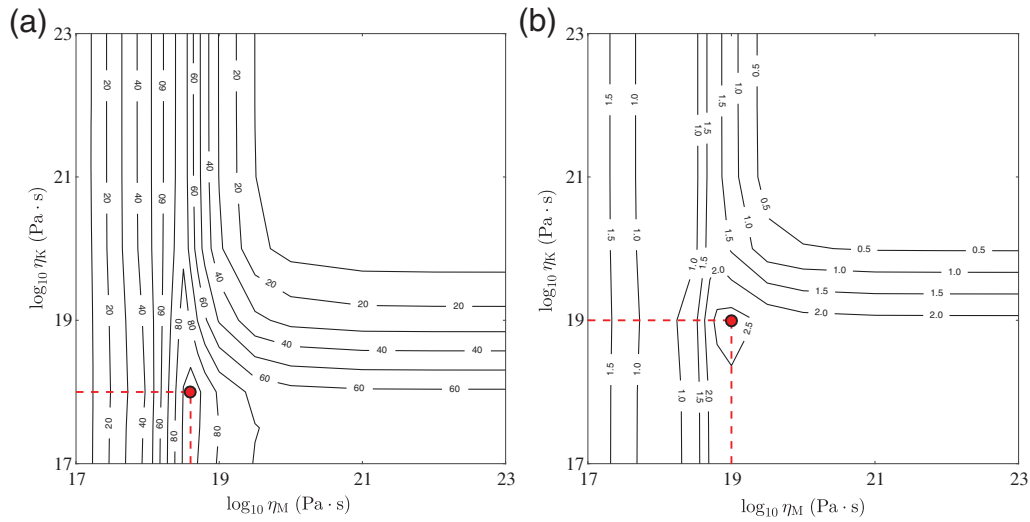


Figure 6. (a) Contour plot of mean residual improvement (MRI; equation 11) as a function of assumed viscosity structure for the post-seismic GPS data from TUBI. The viscosity structure that allows the model to fit the data best, a Maxwell viscosity $\eta_M = 10^{18.6}$ Pa·s and a Kelvin viscosity $\eta_K = 10^{18.0}$ Pa·s, is highlighted by a red circle. This model fits the time series with a mean residual displacement of 3.27 mm, which corresponds to an MRI of 95.16%. (b) Contour plot of MRI (equation 11) as a function of assumed viscosity structure for the interseismic GPS data from 1988 to 1999 (Reilinger *et al.*, 2006), before the İzmit earthquake. The viscoelastic block models best explain the GPS velocity field with a Maxwell viscosity $\eta_M = 10^{19.0}$ Pa·s and a Kelvin viscosity $\eta_K = 10^{19.0}$ Pa·s. This best-fit model is indicated by a red circle and explains the corrected interseismic velocity field $\mathbf{v}_*(\eta_M, \eta_K)$ (equation 8) with a mean residual velocity of 3.14 mm/yr, which corresponds to an MRI of 2.73%.

ments due to the postseismic perturbation only for an elastic model are 0.

The model with the best-fit viscosity structure ($\eta_M = 10^{18.6}$ Pa·s and $\eta_K = 10^{18.0}$ Pa·s) explains the post-seismic time series with a mean residual displacement of 3.27 mm, which corresponds to an MRI of 95.16% (Figs. 4a and 6a). Holding the best-fit Kelvin viscosity constant, an increase in Maxwell viscosity to $\eta_M = 10^{19.0}$ Pa·s decreases the MRI to 79.71% (mean residual displacement of 13.96 mm), whereas a decrease in Maxwell viscosity to $\eta_M = 10^{18.0}$ Pa·s decreases the MRI to 37.25% (mean residual displacement of 42.36 mm) (Fig. 6a). Overall, mean residual displacements are less sensitive to changes in Kelvin viscosity; holding the best-fit Maxwell viscosity constant, an increase in Kelvin viscosity to $\eta_K = 10^{19.0}$ Pa·s corresponds to an MRI of 80.27% (mean residual displacement of 13.31 mm), and a decrease to $\eta_K = 10^{17.0}$ Pa·s corresponds to an MRI of 90.92% (mean residual displacement of 4.00 mm) (Fig. 6a).

Modeling the Pre-İzmit Earthquake Interseismic Velocity Field

We consider 3D block models (Fig. 1) taking into account the viscoelastic effects of historical earthquakes for Maxwell and Kelvin viscosities ranging from $10^{17.0}$ to $10^{23.0}$ Pa·s. These block models also incorporate homogeneous internal block strain (e.g., Meade and Loveless, 2009), and we enforce three tensile slip-rate constraints on the central and southern strands of the NAF in the Sea of Marmara to damp fault normal motion. We summarize the viscoelastic block model results (Figs. 7–10) in six major points.

1. In the models considered here, fault-slip-deficit rate estimates and block model residual velocities are most sensitive to variations in Maxwell viscosity (Fig. 9). Slip-deficit rate estimates along the central and eastern NAF may vary by as much as $\sim 23\%$ (4–5 mm/yr), depending on the assumed Maxwell viscosity (Fig. 9), whereas variations in Kelvin viscosity in the $10^{17.0}$ to $10^{23.0}$ Pa·s range lead to changes of less than 3%–4% ($< \sim 1$ mm/yr) in estimated slip-deficit rates along the central NAF. The relative insensitivity of these results to Kelvin viscosity is likely due to the timing of the historic earthquakes; the most recent earthquake included in the block models occurred in 1967, and the effects of the transient Kelvin viscosity have largely abated after 30 yrs. Because of the difference in sensitivity, we present estimated fault-slip-deficit rates as functions of Maxwell viscosity, at a fixed η_K of $10^{19.0}$ Pa·s (Fig. 9).
2. Slip-deficit rate estimates do not vary monotonically with increases or decreases in assumed Maxwell viscosity (Fig. 9). Assuming a Maxwell viscosity $\eta_M = 10^{20}$ Pa·s and a Kelvin viscosity $\eta_K = 10^{19}$ Pa·s, slip-deficit rate estimates along the central NAF are ~ 22 mm/yr. A decrease in assumed Maxwell viscosity to $\eta_M = 10^{19}$ Pa·s lowers slip-deficit rate estimates to ~ 21 mm/yr, and a further decrease in assumed Maxwell viscosity to $\eta_M = 10^{17}$ Pa·s raises the estimated slip-deficit rate to 24 mm/yr (Fig. 9). The reasons why slip-deficit rate estimates are nonmonotonic functions of Maxwell viscosity can be seen from equation (4). The viscoelastic correction added to the GPS velocity field for a single set of periodic earthquakes is $-\mathbf{v}_{VE}(\eta_M, \eta_K, t - t_{eq}) + \bar{\mathbf{v}}_{VE}(\eta_M, \eta_K, T)$. The earth-

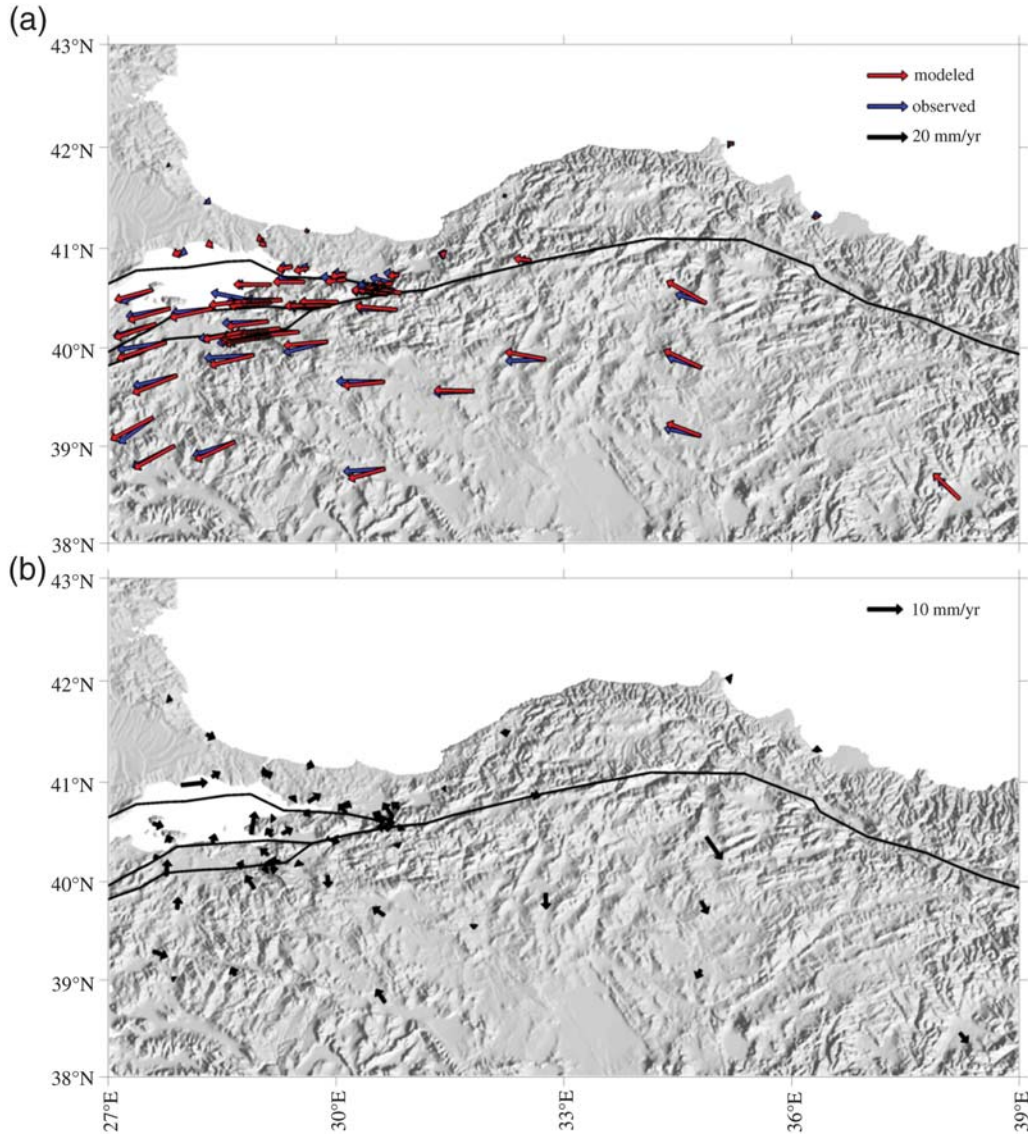


Figure 7. (a) Observed (blue) and modeled (red) interseismic GPS velocity fields for the best-fit viscosity structure highlighted in Figure 6b (Maxwell viscosity $\eta_M = 10^{19.0}$ Pa·s and a Kelvin viscosity $\eta_K = 10^{19.0}$ Pa·s). The observed velocity field shown here is the corrected interseismic velocity field $\mathbf{v}_*(\eta_M, \eta_K)$ (equation 8). (b) Residual velocities for the case shown in (a). Note the different scale from (a).

quakes we take into account in these models (Fig. 5; Table 1) took place between 1 B.C.E. and 1967, and therefore $30 < t - t_{eq} < 1997$ yrs. For low viscosities ($\eta_M < 10^{19}$ Pa·s; $\eta_K < 10^{19}$ Pa·s), after ~ 100 yrs, the first term $-\mathbf{v}_{VE}(\eta_M, \eta_K, t - t_{eq}) \approx 0$ because all stresses are rapidly relaxed, and the mean velocity term $\bar{\mathbf{v}}_{VE}(\eta_M, \eta_K, T)$ dominates the viscoelastic correction. As a result, the viscoelastic correction added to the GPS velocity field is in the same direction as the near-fault velocities, increasing their magnitudes and leading to slip-deficit rate estimates that are generally faster than elastic block model estimates (Fig. 9).

For high viscosities ($\eta_M > 10^{20}$ Pa·s; $\eta_K > 10^{20}$ Pa·s), the magnitudes of the viscoelastic corrections are small compared to the magnitude of the observed GPS velocities.

The mean magnitude of the viscoelastic corrections across all stations for viscosity structures with $\eta_M > 10^{20}$ Pa·s and $\eta_K > 10^{20}$ Pa·s is less than 0.4 mm/yr ($< 3\%$ of the mean magnitude GPS station velocity). As a result, the estimated slip-deficit rates approach elastic block model slip-deficit rates for these high viscosities (Fig. 9).

The slip-deficit rate estimates assuming midrange viscosities (10^{18} Pa·s $< \eta_M < 10^{20}$ Pa·s, 10^{18} Pa·s $< \eta_K < 10^{20}$ Pa·s) are perhaps the most interesting (Fig. 9). These slip-deficit rate estimates depend on the relative magnitudes of the two terms in the viscoelastic corrections for each earthquake. For earthquakes that occurred more than a few centuries ago, $-\mathbf{v}_{VE}(\eta_M, \eta_K, t - t_{eq}) \approx 0$ and $\bar{\mathbf{v}}_{VE}(\eta_M, \eta_K, T)$ are the larger magnitude terms. In this case, for the same reason as low-viscosity cases, the slip-

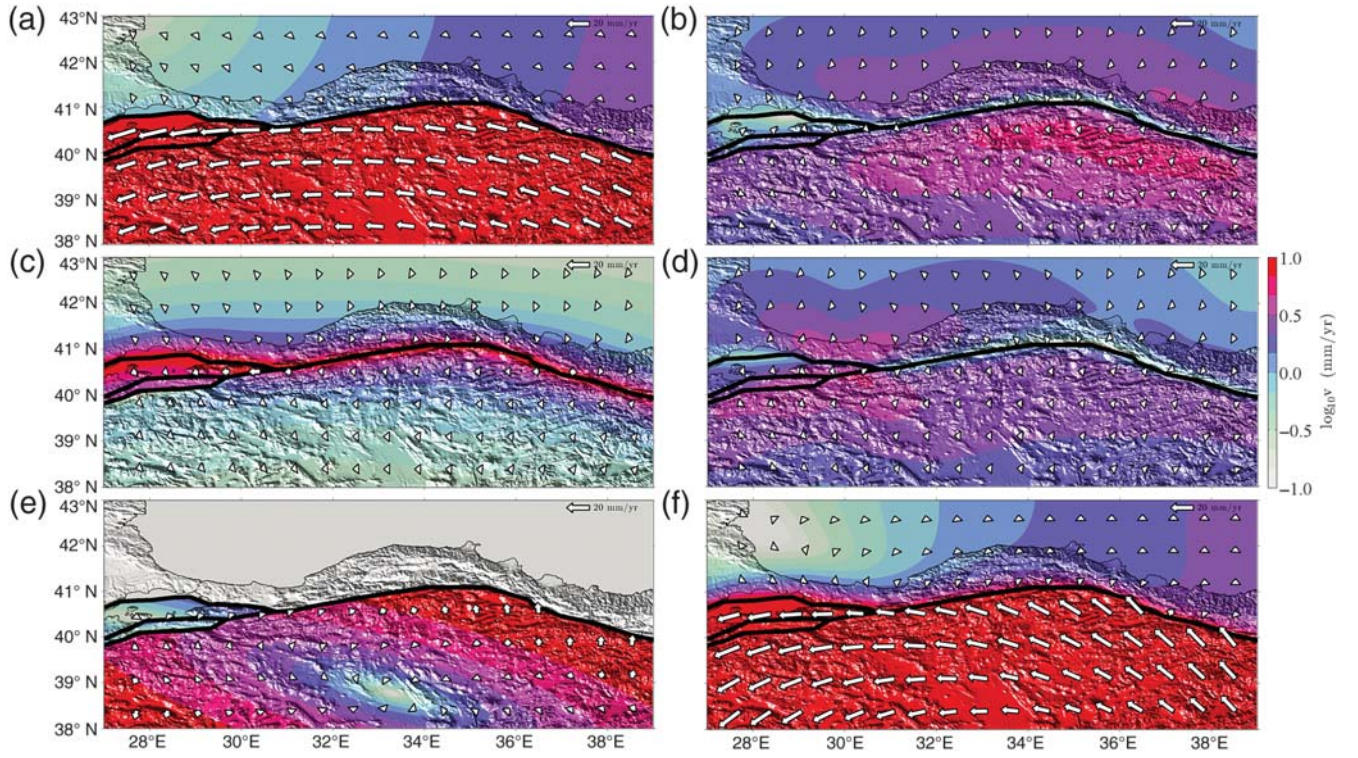


Figure 8. The components of the modeled interseismic velocity field (equation 2) for the best-fit viscoelastic block model (Maxwell viscosity $\eta_M = 10^{19.0}$ Pa·s and a Kelvin viscosity $\eta_K = 10^{19.0}$ Pa·s), with velocity magnitude and direction shown with white arrows and the logarithm of velocity magnitude shown in color to emphasize subtle spatial variations. (a) Velocities due to long-term block motion, (b) the viscoelastic effects of the most recent earthquake along the fault segment, (c) the velocities due to the accumulated slip deficit, (d) the mean velocity throughout the earthquake cycle, and (e) the velocities due to the homogenous intrablock strain. Interseismic velocities (f) are modeled as the sum of the velocity components in (a), (b), (c), and (e) with the mean velocity throughout the earthquake cycle velocity (d) subtracted to ensure that over many earthquake cycles, the displacements everywhere are equal to the long-term block displacements.

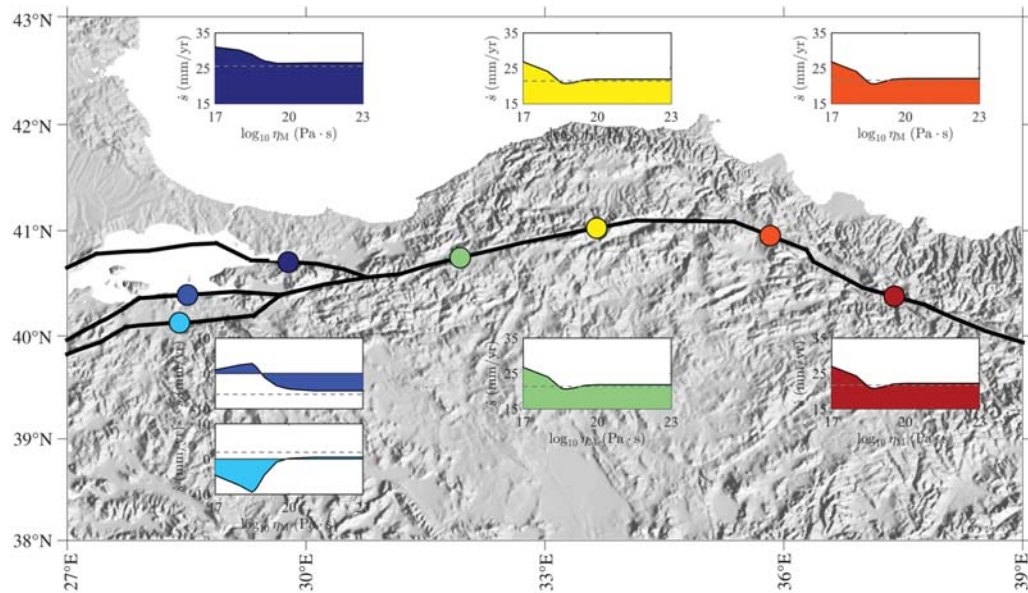


Figure 9. Sensitivity of viscoelastic block model slip-deficit rate estimates to variations in assumed Maxwell viscosity at a fixed Kelvin viscosity of $\eta_K = 10^{19}$ Pa·s for selected fault segments. Dotted gray lines indicate slip-deficit rate estimates from an elastic model with internal strain. In each panel, elastic slip-deficit rates do not coincide exactly with slip-deficit rates at high Maxwell viscosities because the Kelvin viscosity η_K is fixed at 10^{19} Pa·s.

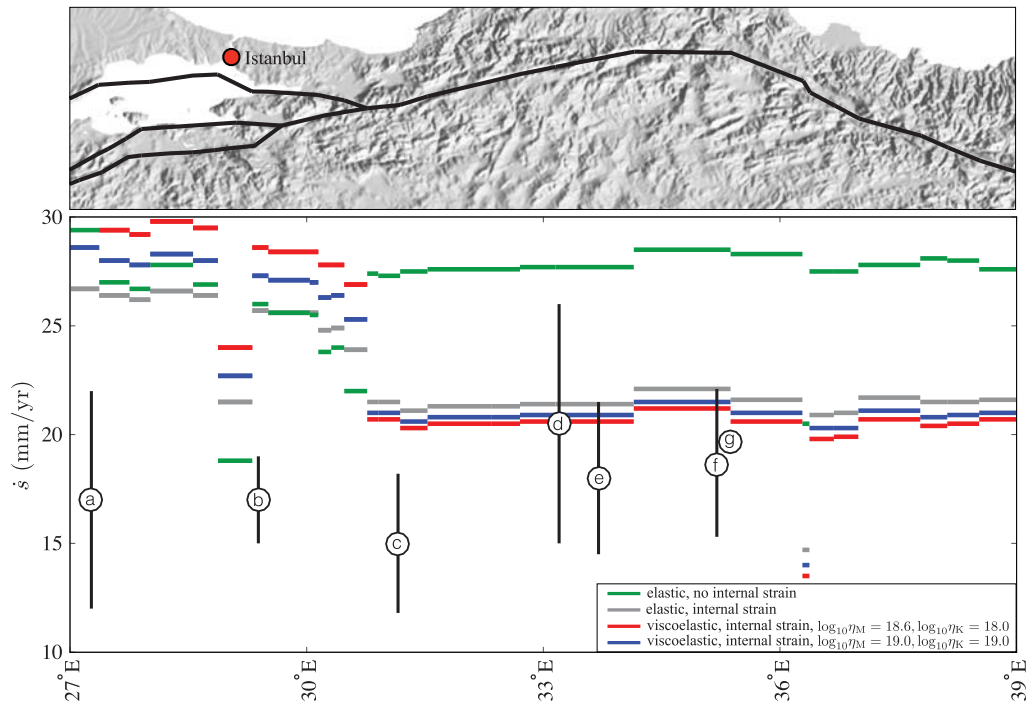


Figure 10. Viscoelastic block model slip-deficit rate estimates along strike assuming the best-fit viscosity structures (Fig. 6): $\eta_M = 10^{19.0}$ Pa·s, $\eta_K = 10^{19.0}$ Pa·s (blue), and $\eta_M = 10^{18.6}$ Pa·s, $\eta_K = 10^{18.0}$ Pa·s (red). For comparison, slip-deficit rates from an elastic block model incorporating internal strain are plotted in gray, and those for an elastic block model with no internal strain are in green. For simplicity, only the slip-deficit rate estimates on the northernmost segments of the fault in the Sea of Marmara region are shown. White circles labeled (a) indicate Meghraoui *et al.* (2012), (b) Dolan *et al.* (2009) and Uçarkuş (unpublished thesis, 2010; see Data and Resources), (c) Pucci *et al.* (2008), (d) Kozacı *et al.* (2007), (e) Hubert-Ferrari *et al.* (2002), (f) Kozacı *et al.* (2009), and (g) Kondo *et al.* (2004), and corresponding error bars represent geologic slip-rate estimates and reported uncertainties.

deficit rate estimates would likely be faster than elastic block model estimates. However, the viscoelastic corrections for the more recent 1939–1967 earthquakes are dominated by $-\mathbf{v}_{VE}(\eta_M, \eta_K, t - t_{eq})$, and therefore the viscoelastic corrections added to the GPS velocity field for these earthquakes are in the opposite direction as the near-fault velocities, decreasing their magnitudes and leading to slip-deficit rate estimates that are slower than elastic block model results (Fig. 9).

3. The incorporation of homogeneous internal block strain has a substantial effect on slip-deficit rate estimates along the entire fault system. Along the central NAF, slip-deficit rate estimates from an elastic block model with no internal strain are ~ 27 – 28 mm/yr, and after incorporating internal strain, these estimates decrease by $\sim 20\%$ to 21 – 22 mm/yr (Fig. 10). Slip-deficit rate variations due to viscoelastic effects assuming the best-fit viscosity structures (Fig. 6) are comparatively small (< 1 – 2 mm/yr; Fig. 10) along the central and eastern NAF. In contrast, the addition of internal block strain leads to an ~ 0.5 – 2.5 mm/yr increase in slip-deficit rate estimates relative to an elastic block model along the northern strand of the NAF in the Sea of Marmara (Fig. 10). Variations in slip-deficit rate due to viscoelastic effects across the best-fit models along this northern strand are of comparable magnitudes (Fig. 10).

4. In the Sea of Marmara region, the variations in estimated slip-deficit rates are complex functions of viscosity structure (Figs. 9 and 10). After incorporating the effects of previous earthquakes with the best-fit viscoelastic structures (Fig. 6b), slip-deficit rate estimates decrease by 1 – 2 mm/yr along the central NAF, but increase on the northern strand of the western NAF by a more substantial ~ 2 – 3 mm/yr (Fig. 9). The slip-deficit rate differential between the northern Sea of Marmara strand and the central NAF is the largest after taking into account both internal block strain and viscoelastic effects; slip-deficit rate estimates on the northern strand, less than 50 km from Istanbul, are $\sim 20\%$ faster than slip-deficit rate estimates along the central NAF for viscoelastic block models with the best-fit viscosity structures (Fig. 6b) but only $\sim 15\%$ faster for an elastic model with internal strain (Fig. 10). In addition, the senses of slip on the two southern Sea of Marmara strands reverse depending on assumed viscosity structure. In the elastic limit, the middle strand of the NAF that runs along the southern coast of the Sea of Marmara is right lateral with a slip-deficit rate of ~ 5 mm/yr and the southernmost strand of the NAF is left lateral with a slip-deficit rate of < 1 mm/yr. For Maxwell viscosities $\eta_M < 10^{20.0}$ Pa·s, the sense of slip on the southernmost strand becomes left lateral, and for Maxwell viscosities $\eta_M < 10^{18.7}$ Pa·s, the sense of slip on the middle strand

becomes right lateral. The trade-off in slip sense between the two southern strands is largely due to the complicated fault geometry in this region and sparse geodetic observations due to the location of the Sea of Marmara (Fig. 1). The most distinct gradient in GPS velocities occurs across the northern strand of the NAF (Fig. 1); farther south, the velocity gradient is less distinct, allowing a trade-off in slip sense between the two southern NAF strands.

5. Overall, the viscosity structure that best explains the interseismic GPS data from 1988 to 1999 (Reilinger *et al.*, 2006), before the İzmit earthquake, is a Maxwell viscosity $\eta_M = 10^{19.0}$ Pa·s and a Kelvin viscosity $\eta_K = 10^{19.0}$ Pa·s (Figs. 6b, 7, and 8). This model fits the corrected interseismic velocity field $\mathbf{v}_*(\eta_M, \eta_K)$ (equation 9) with a mean residual velocity of 3.14 mm/yr, which corresponds to an MRI (equation 10) of 2.73% (Figs. 6b and 7).
6. Slip-deficit rate estimates and changes in block model residuals are most sensitive to the earthquakes that occurred since 1500 C.E. Removing the effects of the pre-1500 C.E. earthquakes does not change the major conclusions of this article. Estimated slip-deficit rates change by less than ~ 2 mm/yr (Ⓔ Fig. S1, available in the electronic supplement to this article) and the best-fit viscosity structure for the interseismic GPS data changes slightly from $\eta_M = 10^{19.0}$ Pa·s and $\eta_K = 10^{19.0}$ Pa·s to $\eta_M = 10^{18.8}$ Pa·s and $\eta_K = 10^{19.0}$ Pa·s (Ⓔ Fig. S2).

Discussion

We have systematically modeled both pre- and post-İzmit observations with two-layer Burgers viscoelastic models with Maxwell and Kelvin viscosities ranging from $10^{17.0}$ to $10^{23.0}$ Pa·s. The viscosity structure that best explains the TUBI postseismic data is a Maxwell viscosity $\eta_M = 10^{18.6}$ Pa·s and a Kelvin viscosity $\eta_K = 10^{18.0}$ Pa·s (Fig. 6a), and the viscosity structure that best explains the interseismic data is a Maxwell viscosity $\eta_M = 10^{19.0}$ Pa·s and a Kelvin viscosity $\eta_K = 10^{19.0}$ Pa·s (Fig. 6b).

A comparison of the MRI values for the pre- and post-earthquake data as a function of viscosity structure (Fig. 6) reveals that the two best-fit models are remarkably similar, and both sets of data may be explained with a single geodetically constrained Burgers rheology of $\eta_M = 10^{18.6}$ – $10^{19.0}$ Pa·s and $\eta_K = 10^{18.0}$ – $10^{19.0}$ Pa·s. The variation in slip-deficit rate estimates along the central NAF for viscosities within this best-fit range is < 1 mm/yr (Fig. 10). An elastic block model that incorporates homogenous internal block strain, but does not incorporate viscoelasticity, yields slip-deficit rate estimates that are 1.0–1.5 mm/yr faster than the best-fit viscoelastic models along the central NAF (Fig. 9). For comparison, an elastic block model that does not incorporate both homogenous strain and viscoelasticity leads to slip-deficit rate estimates that are 5 mm/yr faster along the central NAF than an elastic model incorporating internal strain (Fig. 9).

The viscoelastic block model results (Figs. 9 and 10) suggest that slip-deficit rate estimates along the central NAF

(31°E – 38°E ; Fig. 1) with a geodetically constrained rheology of $\eta_M = 10^{18.6}$ – $10^{19.0}$ Pa·s and $\eta_K = 10^{18.0}$ – $10^{19.0}$ Pa·s are only 1–2 mm/yr (5%–10%) slower than those of an analogous elastic block model that incorporates internal block strain (Fig. 10). Conversely, on the northern strand of the NAF in the Sea of Marmara, slip-deficit rate estimates with the geodetically constrained rheology are significantly faster (2–3 mm/yr or 10%–15%) than slip-deficit rates from an elastic model that incorporates internal strain. Slip-deficit rate estimates along the northern strand of the NAF, after accounting for viscoelastic effects with the geodetically constrained rheology, are the fastest in the entire fault system (27–28 mm/yr; Fig. 10). In other words, the viscoelastic effects of historical earthquakes, when not accounted for, may partially mask very fast (~ 27 – 28 mm/yr) slip-deficit rates along the northern strand of the NAF. The slip-deficit rate estimates along the northern strand of the NAF are especially significant, because it runs less than 50 km from Istanbul, a city with more than 14 million people.

The geodetically constrained rheology can explain both the pre-İzmit nominally interseismic (late in the earthquake cycle) GPS velocities and the postseismic (early in the earthquake cycle) displacements from GPS station TUBI (Fig. 6). The goal of explaining geodetic observations from across the earthquake cycle is to develop unified earthquake cycle models that can simultaneously provide a physical explanation for both rapid postseismic deformation and more slowly varying, nominally interseismic, deformation (Hetland, 2006; Meade *et al.*, 2013). Previous viscosity structures estimated based on both pre- and postearthquake geodetic observations along the NAF (transient relaxation timescale $\tau_K = \eta_K/\mu_K$ of 2–5 yrs, corresponding to a Kelvin viscosity η_K of $\sim 0.8 \times 10^{18}$ to $\sim 1.9 \times 10^{18}$ Pa·s for the shear modulus used here, and a steady timescale of $\tau_M = \eta_M/\mu_M$ of more than 400 yrs, corresponding to a Maxwell viscosity η_M of $\sim 1.5 \times 10^{20}$ Pa·s; Hetland, 2006) may be slightly higher than the best-fit viscosities found here (Fig. 6) but are not directly analogous to the present study, because they are based on 2D modeling without a block model framework or internal block strain. To explain both the postseismic deformation and the pre-earthquake velocity gradient across the NAF observed before 1999, a subsequent study suggested that a combination of afterslip and a Burgers rheology with two viscosities (2 – 5×10^{19} Pa·s and at least 2×10^{20} Pa·s) might be necessary (Hearn *et al.*, 2009).

Geodetic observations across strike-slip faults from both early and late in the earthquake cycle now exist at several locations worldwide. In Tibet, Interferometric Synthetic Aperture Radar (InSAR) and GPS measurements across the Kunlun fault in Tibet reveal localized velocity profiles with differential velocities of ~ 3 and ~ 12 mm/yr across the faults prior to the 1997 M_w 7.6 Manyi (Bell *et al.*, 2011) and 2001 M_w 7.8 Kokoxili (Zhang *et al.*, 2004) earthquakes, respectively. After these Tibet earthquakes, GPS and InSAR data recorded postseismic motions up to 10 times larger in magnitude than pre-earthquake velocities (Ryder *et al.*, 2007,

2011; Zhang *et al.*, 2009). In 2D, geodetic data from both early and late in the earthquake cycle in Tibet have been modeled with layered Maxwell models (DeVries and Meade, 2013), and more globally, geodetic data from across 15 strike-slip faults worldwide are consistent with a 2D, two-layer Burgers model (Meade *et al.*, 2013). More recently, localized shear zones have been used to explain representative velocity profiles before and after large strike-slip earthquakes (Hearn and Thatcher, 2015) as well as data from before and after the İzmit earthquake (Yamasaki *et al.*, 2014).

Along the central and eastern NAF, previous geodetic slip-deficit rate estimates (e.g., Reilinger *et al.*, 1997, 2006; McClusky *et al.*, 2000) were $\sim 1\text{--}10$ mm/yr faster than geologic slip-rate estimates (Fig. 10; e.g., Hubert-Ferrari *et al.*, 2002; Okumura *et al.*, 2003; Kondo *et al.*, 2004; Kozacı *et al.*, 2007, 2009). This discrepancy may be partially explained if the geologic slip-rate estimates are considered to be minimum bounds (Kozacı *et al.*, 2007; Dolan, 2009). However, here, after taking into account internal block strain and the viscoelastic effects of historic earthquakes along the NAF, the discrepancy between geodetic slip-deficit rate and geologic slip-rate estimates decreases along the central NAF; indeed, the geodetic slip-deficit rate is, within error, the same as the fastest geological slip rate of 21.5 ± 5.5 mm/yr (Kozacı *et al.*, 2007) along the central NAF (Fig. 10), suggesting that there may be no discrepancy between the different rates along this part of the system.

Finally, the NAF is often considered to be a seismically active analog of the SAF system in California; the fault systems are of similar size and both delineate major transform plate boundaries. Recent viscoelastic block modeling studies focused on California have suggested that faults that are late in the earthquake cycle may have higher slip rates than previously estimated in classic block models (Johnson *et al.*, 2007; Chuang and Johnson, 2011; Hearn *et al.*, 2013; Tong *et al.*, 2014). These results are perhaps analogous to the results of the present study along the western NAF, where slip-rate estimates from a viscoelastic block model are 2–5 mm/yr higher than those from an elastic model (Fig. 10).

Conclusions

GPS data from both before and after the 1999 İzmit earthquake may be simultaneously explained with a two-layer Burgers rheology incorporated into 3D block models with $\eta_M = 10^{18.6}\text{--}10^{19.0}$ Pa·s and $\eta_K = 10^{18.0}\text{--}10^{19.0}$ Pa·s in the lower layer. Viscoelastic block models of the interseismic velocity field observed prior to the 1999 earthquake fit the GPS data best with a viscosity structure of $\eta_M = 10^{19.0}$ Pa·s and $\eta_K = 10^{19.0}$ Pa·s, and the TUBI postseismic data are best explained by a two-layer viscoelastic model with $\eta_M = 10^{18.6}$ Pa·s and $\eta_K = 10^{18.0}$ Pa·s. In addition to a unified description of surface deformation prior to and after a large strike-slip earthquake, these viscoelastic block model results suggest that: (1) the fastest slip-deficit rate estimates along the entire fault system ($\sim 27\text{--}28$ mm/yr) occur along the

northern strand of the NAF in the Sea of Marmara, less than 50 km from Istanbul; (2) slip-deficit rate estimates do not vary monotonically with Maxwell viscosity along the central and eastern NAF; (3) the senses of slip on the two NAF strands in the southern Sea of Marmara region reverse depending on assumed Maxwell viscosity; (4) slip-deficit rate estimates from viscoelastic block models with a geodetically constrained rheology along the central and eastern NAF are 1–2 mm/yr slower than equivalent elastic models; and (5) after taking into account internal block strain and the viscoelastic effects of historic earthquakes with the best-fit viscosities estimated here, the discrepancy between the geodetic slip-deficit rate estimates and geologic slip-rate estimates decreases along the central NAF.

Data and Resources

All data used in this article came from published sources listed in the references. The computations in this article were run on the Odyssey cluster supported by the Faculty of Arts and Sciences (FAS) Division of Science Research Computing Group at Harvard University. This study used the following numerical inverse Laplace transform written by K. J. Hollenbeck in 1998, INVLAP.M: A MATLAB function for numerical inversion of Laplace transforms by the de Hoog algorithm (https://www.mathworks.com/matlabcentral/answers/uploaded_files/1034/invlap.m), last accessed November 2016). Finally, the detailed citation for the reference Uçarkuş (unpublished thesis, 2010) in the main text is G. Uçarkuş (2010), Active faulting and earthquake scarps along the North Anatolian fault in the Sea of Marmara, unpubl. Ph.D. Thesis, Istanbul Technical University, Istanbul, Turkey.

Acknowledgments

We thank Jeff Freymueller, an anonymous reviewer, and Associate Editor William Hammond for thoughtful reviews that led to substantial improvements. This work was supported by Harvard University and the Department of Energy Computational Science Graduate Fellowship Program of the Office of Science and National Nuclear Security Administration in the Department of Energy under Contract DE-FG02-97ER25308.

References

- Ambraseys, N. (2001). The earthquake of 10 July 1894 in the Gulf of İzmit (Turkey) and its relation to the earthquake of 17 August 1999, *J. Seismol.* **5**, 117–128.
- Ambraseys, N. (2002). The seismic activity of the Marmara Sea region over the last 2000 years, *Bull. Seismol. Soc. Am.* **92**, no. 1, 1–18.
- Ambraseys, N. N., and J. A. Jackson (2000). Seismicity of the Sea of Marmara (Turkey) since 1500, *Geophys. J. Int.* **141**, F1–F6.
- Bakun, W. H., and A. G. Lindh (1985). The Parkfield, California, earthquake prediction experiment, *Science* **229**, no. 4714, 619–624.
- Barka, A. (1992). The North Anatolian fault zone, special issue, *Ann. Tect.* **IV** (Suppl.), 164–195.
- Barka, A. (1996). Slip distribution along the North Anatolian fault associated with the large earthquakes of the period 1939 to 1967, *Bull. Seismol. Soc. Am.* **86**, no. 5, 1238–1254.
- Barka, A. (1999). The 17 August 1999 İzmit earthquake, *Science* **285**, no. 5435, 1858–1859.

- Bell, M. A., J. R. Elliott, and B. E. Parsons (2011). Interseismic strain accumulation across the Manyi (Tibet) prior to the 1997 M_w 7.6 earthquake, *Geophys. Res. Lett.* **38**, L24302, doi: [10.1029/2011GL049762](https://doi.org/10.1029/2011GL049762).
- Bürgmann, R., S. Ergintav, P. Segall, E. Hearn, S. McClusky, R. E. Reilinger, H. Woith, and J. Zschau (2002). Time-dependent distributed afterslip on and deep below the İzmit earthquake rupture, *Bull. Seismol. Soc. Am.* **92**, no. 1, 126–137.
- Chopra, P. N. (1997). High-temperature transient creep in olivine rocks, *Tectonophysics* **279**, 93–111.
- Chuang, R. Y., and K. M. Johnson (2011). Reconciling geologic and geodetic model fault slip-rate discrepancies in southern California: Consideration of nonsteady mantle flow and lower crustal fault creep, *Geology* **37**, no. 7, 627–630.
- de Hoog, F. R., J. H. Knight, and A. N. Stokes (1982). An improved method for numerical inversion of Laplace transforms, *SIAM J. Sci. Stat. Comput.* **3**, 357–366.
- DeVries, P. M. R., and B. J. Meade (2013). Earthquake cycle deformation in the Tibetan plateau with a weak mid-crustal layer, *J. Geophys. Res.* **118**, 3101–3111.
- Dolan, J. F. (2009). Accelerated strain accumulation along the western North Anatolian fault: A possible precursory signal to an impending earthquake, *American Geophysical Union Fall Meeting Abstract T13D-1920*, San Francisco, California, 14–18 December.
- Dolan, J., Ö. Kozacı, and R. Hartleb (2009). Paleoseismology of the North Anatolian fault: Implications for earthquake occurrence and seismic hazard assessment, *Proc. of the International Symposium on Historical Earthquakes and Conservation of Monuments and Sites in the Eastern Mediterranean Region, 500th Anniversary Year of the 1509 September 10 Marmara Earthquake*, 10–12 September 2009, Istanbul Technical University Press, Istanbul, Turkey, 30–33.
- Drab, L., A. Hubert-Ferrari, S. Schmidt, P. Martinez, J. Carlut, and M. El Ouahabi (2015). Submarine earthquake history of the Çınarcık segment of the North Anatolian Fault in the Marmara Sea, Turkey, *Bull. Seismol. Soc. Am.* **105**, no. 2A, 622–645.
- Ergintav, S., R. Bürgmann, S. McClusky, C. Çakmak, R. E. Reilinger, O. Lenk, A. Barka, and H. Özener (2002). Postseismic deformation near the İzmit earthquake (17 August 1999, $M = 7.5$) rupture zone, *Bull. Seismol. Soc. Am.* **92**, no. 1, 194–207.
- Ergintav, S., S. McClusky, E. Hearn, R. Reilinger, C. Çakmak, T. Herring, H. Özener, O. Lenk, and E. Tari (2009). Seven years of postseismic deformation following the 1999, $M = 7.4$ and $M = 7.2$, İzmit-Düzce, Turkey earthquake sequence, *J. Geophys. Res.* **114**, no. B07403, doi: [10.1029/2008JB006021](https://doi.org/10.1029/2008JB006021).
- Fukahata, Y., and M. Matsu'ura (2005). General expressions for internal deformation fields due to a dislocation source in a multilayered elastic half-space, *Geophys. J. Int.* **161**, 507–521.
- Fukahata, Y., and M. Matsu'ura (2006). Quasi-static internal deformation due to a dislocation source in a multilayered elastic/viscoelastic half-space and an equivalent theorem, *Geophys. J. Int.* **166**, 418–432.
- Hashima, A., M. Fukahata, C. Hashimoto, and M. Matsu'ura (2014). Quasi-static strain and stress fields due to a moment tensor in elastic-viscoelastic layered half-space, *Pure Appl. Geophys.* **171**, 1669–1693.
- Hearn, E. H., and W. R. Thatcher (2015). Reconciling viscoelastic models of postseismic and interseismic deformation: Effects of viscous shear zones and finite-length ruptures, *J. Geophys. Res.* **120**, no. 4, 2794–2819.
- Hearn, E. H., R. Bürgmann, and R. E. Reilinger (2002). Dynamics of İzmit earthquake postseismic deformation and loading of the Düzce earthquake hypocenter, *Bull. Seismol. Soc. Am.* **92**, 172–193.
- Hearn, E. H., S. McClusky, S. Ergintav, and R. E. Reilinger (2009). İzmit earthquake postseismic deformation and dynamics of the North Anatolian fault zone, *J. Geophys. Res.* **114**, no. B08405, doi: [10.1029/2008JB006026](https://doi.org/10.1029/2008JB006026).
- Hearn, E. H., C. T. Onishi, F. F. Pollitz, and W. R. Thatcher (2013). How do “ghost transients” from past earthquakes affect GPS slip rate estimates on southern California faults?, *Geochem. Geophys. Geosyst.* **14**, no. 4, 828–838.
- Hetland, E. A. (2006). Models of interseismic deformation with an analytic framework for the inclusion of general linear viscoelastic rheologies, *Ph.D. Thesis*, Massachusetts Institute of Technology, Cambridge, Massachusetts.
- Hetland, E. A., and B. H. Hager (2005). Postseismic and interseismic displacements near a strike-slip fault: A two-dimensional theory for general linear viscoelastic rheologies, *J. Geophys. Res.* **110**, no. B10401, doi: [10.1029/2005JB003689](https://doi.org/10.1029/2005JB003689).
- Hetland, E. A., and B. H. Hager (2006). The effects of rheological layering on post-seismic deformation, *Geophys. J. Int.* **166**, 277–292.
- Hildebrand, F. B. (1987). *Introduction to Numerical Analysis*, Second Ed., Dover Publications, Mineola, New York, 704 pp.
- Hilley, G. E., K. M. Johnson, M. Wang, Z.-K. Shen, and R. Bürgmann (2009). Earthquake-cycle deformation and fault slip rates in northern Tibet, *Geology* **37**, no. 1, 31–34.
- Hubert-Ferrari, A., R. Armijo, G. King, B. Meyer, and A. Barka (2002). Morphology, displacement, and slip rates along the North Anatolian fault, Turkey, *J. Geophys. Res.* **107**, no. B10, 2235.
- Johnson, K. M., G. E. Hilley, and R. Bürgmann (2007). Influence of lithosphere viscosity structure on estimates of fault slip rate in the Mojave region of the San Andreas fault system, *J. Geophys. Res.* **112**, no. B07408.
- Klöckner, A., A. Barnett, L. Greengard, and M. O'Neil (2013). Quadrature by expansion: A new method for the evaluation of layer potentials, *J. Comput. Phys.* **252**, 332–349.
- Kondo, H., V. Özaksay, C. Yildirim, Y. Awata, Ö. Emre, and K. Okumura (2004). 3D trenching survey at Demir Tepe site on the 1944 Bolu-Gerede earthquake ruptures, North Anatolian fault system, Turkey, *Seismol. Res. Lett.* **75**, no. 2, 292.
- Kozacı, Ö., J. Dolan, and R. Finkel (2009). A late Holocene slip rate for the central North Anatolian fault, at Tahtaköprü Turkey, from cosmogenic ^{10}Be geochronology: Implications for fault loading and strain release rates, *J. Geophys. Res.* **114**, no. B01405, doi: [10.1029/2008JB005760](https://doi.org/10.1029/2008JB005760).
- Kozacı, Ö., J. Dolan, R. Finkel, and R. Hartleb (2007). Late Holocene slip rate for the North Anatolian fault, Turkey, from cosmogenic ^{36}Cl geochronology: Implications for the constancy of fault loading and strain release rates, *Geology* **35**, no. 10, 867–870.
- Lorenzo-Martin, F., F. Roth, and R. Wang (2006). Elastic and inelastic triggering of earthquakes in the North Anatolian fault zone, *Tectonophysics* **424**, 271–289.
- Matsu'ura, M., and R. Sato (1975). Static deformation due to the fault spreading over several layers in a multi-layered medium, part II: Strain and tilt, *J. Phys. Earth* **23**, 1–29.
- Matsu'ura, M., and T. Sato (1989). A dislocation model for the earthquake cycle at convergent plate boundaries, *Geophys. J. Int.* **96**, 23–32.
- Matsu'ura, M., D. D. Jackson, and A. Cheng (1986). Dislocation model for aseismic crustal deformation at Hollister, California, *J. Geophys. Res.* **91**, no. B12, 12,661–12,674.
- McCaffrey, R. (2002). Crustal block rotations and plate coupling, in *Plate Boundary Zones*, S. Stein and J. T. Freymueller (Editors), in *Geodyn. Ser.*, Vol. 30, AGU, Washington, D.C., 101–122, doi: [10.1029/GD030p0101](https://doi.org/10.1029/GD030p0101).
- McClusky, S. C., S. C. Bjornstad, B. H. Hager, R. W. King, B. J. Meade, M. M. Miller, F. C. Monastero, and B. J. Souter (2000). Global Positioning System constraints on plate kinematics and dynamics in the eastern Mediterranean and Caucasus, *J. Geophys. Res.* **105**, 5695–5719.
- Meade, B. J., and B. H. Hager (2005). Block models of crustal motion in southern California constrained by GPS measurements, *J. Geophys. Res.* **110**, no. B03403, doi: [10.1029/2004JB003209](https://doi.org/10.1029/2004JB003209).
- Meade, B. J., and J. P. Loveless (2009). Block modeling with connected fault-network geometries and a linear elastic coupling estimator in spherical coordinates, *Bull. Seismol. Soc. Am.* **99**, no. 6, 3124–3139.
- Meade, B. J., B. H. Hager, S. C. McClusky, R. E. Reilinger, S. Ergintav, O. Lenk, A. Barka, and H. Özener (2002). Estimates of seismic potential in the Marmara Sea region from block models of secular deformation constrained by Global Positioning System measurements, *Bull. Seismol. Soc. Am.* **92**, no. 1, 208–215.
- Meade, B. J., Y. Klinger, and E. A. Hetland (2013). Inference of multiple earthquake-cycle relaxation timescales from irregular geodetic sampling of interseismic deformation, *Bull. Seismol. Soc. Am.* **103**, no. 5, 2824–2835.

- Meghraoui, M., M. E. Aksoy, H. S. Akyüz, M. Ferry, A. Dikbaş, and E. Altunel (2012). Paleoseismology of the North Anatolian fault at Guzelkoy (Ganos segment, Turkey): Size and recurrence time of earthquake ruptures west of the Sea of Marmara, *Geochem. Geophys. Geosyst.* **13**, no. 4, 1–26.
- Nur, A., and G. Mavko (1974). Postseismic viscoelastic rebound, *Science* **183**, 204–206.
- Okada, Y. (1992). Interl deformation due to shear and tensile faults in a half-space, *Bull. Seismol. Soc. Am.* **82**, no. 2, 1018–1040.
- Okumura, K., T. K. Rockwell, T. Duman, F. Tokay, H. Kondo, C. Yoldirim, and V. Ozaksoy (2003). Refined slip history of the North Anatolian fault at Gerede on the 1944 rupture, *American Geophysical Union Fall Meeting Abstract S12B-0384*, San Francisco, California, 8–12 December.
- Pollitz, F. F. (1992). Postseismic relaxation theory on a spherical earth, *Bull. Seismol. Soc. Am.* **82**, no. 1, 422–453.
- Pollitz, F. F., P. McCrory, J. Svarc, and J. Murray (2008). Dislocation models of interseismic deformation in the western United States, *J. Geophys. Res.* **113**, no. B4, doi: [10.1029/2007JB005174](https://doi.org/10.1029/2007JB005174).
- Pollitz, F. F., P. McCrory, D. Wilson, J. Svarc, C. Puskas, and R. B. Smith (2010). Viscoelastic-cycle model of interseismic deformation in the northwestern United States, *Geophys. J. Int.* **181**, no. 2, 665–696.
- Pucci, S., P. M. De Martini, and D. Pantosti (2008). Preliminary slip rate estimates for the Düzce segment of the North Anatolian fault zone from offset geomorphic markers, *Geomorphology* **97**, no. 3, 538–554.
- Reilinger, R., S. C. McClusky, M. B. Oral, R. W. King, M. N. Toksoz, A. A. Barka, I. Kinik, O. Lenk, and I. Sanli (1997). Global Positioning System measurements of present-day crustal movements in the Arabia-Africa-Eurasia plate collision zone, *J. Geophys. Res.* **102**, 9983–9999.
- Reilinger, R., S. McClusky, P. Vernant, S. Lawrence, S. Ergintav, R. Cakmak, H. Ozener, F. Kadirov, I. Guiliev, R. Stepanyan, *et al.* (2006). GPS constraints on continental deformation in the Africa–Arabia–Eurasia continental collision zone and implications for the dynamics of plate interactions, *J. Geophys. Res.* **111**, no. B5, doi: [10.1029/2005JB004051](https://doi.org/10.1029/2005JB004051).
- Reilinger, R. E., S. Ergintav, R. Bürgmann, S. McClusky, O. Lenk, A. Barka, O. Gurkan, L. Hearn, K. L. Feigl, R. Cakmak, *et al.* (2000). Coseismic and postseismic fault slip for the 17 August, $M = 7.5$, İzmit, Turkey earthquake, *Science* **289**, no. 5484, 1519–1524.
- Ryder, I., R. Bürgmann, and F. Pollitz (2011). Lower crustal relaxation beneath the Tibetan plateau and Qaidam basin following the 2001 Kokoxili earthquake, *Geophys. J. Int.* **187**, 613–630.
- Ryder, I., B. Parson, T. J. Wright, and G. J. Funning (2007). Post-seismic motion following the 1997 Manyi (Tibet) earthquake: InSAR observations and modeling, *Geophys. J. Int.* **169**, no. 3, 1009–1027.
- Sato, R. (1971). Crustal deformation due to dislocation in a multi-layered medium, *J. Phys. Earth* **19**, no. 1, 31–46.
- Sato, R., and M. Matsu'ura (1973). Static deformation due to the fault spreading over several layers in a multi-layered medium, part I: Displacement, *J. Phys. Earth* **21**, 227–249.
- Sato, T., and M. Matsu'ura (1988). A kinematic model for deformation of the lithosphere at subduction zones, *J. Geophys. Res.* **93**, no. B6, 6410–6418.
- Savage, J. C., and R. O. Burford (1973). Geodetic determination of relative plate motion in central California, *J. Geophys. Res.* **78**, no. 5, 832–845.
- Savage, J. C., and W. H. Prescott (1978). Asthenosphere readjustment and the earthquake cycle, *J. Geophys. Res.* **83**, no. B7, 3369–3376.
- Smith, B. R., and D. T. Sandwell (2006). A model of the earthquake cycle along the San Andreas fault system for the past 1000 years, *J. Geophys. Res.* **111**, no. B1, doi: [10.1029/2005JB003703](https://doi.org/10.1029/2005JB003703).
- Stein, R. S., A. A. Barka, and J. H. Dieterich (1997). Progressive failure on the North Anatolian fault since 1939 by earthquake stress triggering, *Geophys. J. Int.* **128**, no. 3, 594–604.
- Straub, C., H. Kahle, and C. Schindler (1997). GPS and geologic estimates of the tectonic activity in the Marmara Sea region, NW Anatolia, *J. Geophys. Res.* **102**, no. B12, 27,587–27,601.
- Toksöz, M. N., A. F. Shakal, and A. J. Michael (1979). Space–time migration of earthquakes along the North Anatolian fault zone and seismic gaps, *Pure App. Geophys.* **117**, 1258–1270.
- Tong, X., B. R. Smith-Konter, and D. T. Sandwell (2014). Is there are discrepancy between geological and geodetic slip rates along the San Andreas fault system? *J. Geophys. Res.* **119**, no. B010765.
- Wang, L., R. Wang, F. Roth, B. Enescu, S. Hainzl, and S. Ergintav (2008). Afterslip and viscoelastic relaxation following the 1999 M 7.4 İzmit earthquake from GPS measurements, *Geophys. J. Int.* **178**, 1220–1237.
- Yamasaki, T., T. J. Wright, and G. A. Houseman (2014). Weak ductile shear zone beneath a major strike-slip fault: Inferences from earthquake cycle model constrained by geodetic observations of the western North Anatolian fault zone, *J. Geophys. Res.* **119**, 3678–3699.
- Zhang, C., J. Cao, and Y. Shi (2009). Studying the viscosity of lower crust of Qinghai-Tibet plateau according to post-seismic deformation, *Sci. China Earth Sci.* **5**, no. 3, 411–419.
- Zhang, P.-Z., Z. Shen, M. Wang, W. Gan, R. Bürgmann, P. Molnar, Q. Wang, Z. Niu, J. Sun, J. Wu, *et al.* (2004). Continuous deformation of the Tibetan plateau from global positioning system data, *Geology* **32**, no. 9, 809–812.

Department of Earth and Planetary Sciences
20 Oxford Street
Cambridge, Massachusetts 02138
phoeberobinson@fas.harvard.edu
meade@fas.harvard.edu
(P.M.R.D., B.J.M.)

Research Computing
Harvard University
38 Oxford Street
Cambridge, Massachusetts 02138
plamenkrastev@fas.harvard.edu
(P.G.K.)

Department of Earth Sciences
Zumberge Hall of Science (ZHS)
University of Southern California
3651 Trousdale Parkway
Los Angeles, California, 90089
dolan@usc.edu
(J.F.D.)

Manuscript received 24 February 2016;
Published Online 29 November 2016